

# Fermi velocity and magic angle renormalization in twisted bilayer graphene

Miguel Sánchez Sánchez<sup>1</sup>, José González<sup>2</sup>, and Tobias Stauber<sup>1</sup>

<sup>1</sup> Instituto de Ciencia de Materiales de Madrid, CSIC, E-28049 Madrid, Spain

<sup>2</sup> Instituto de Estructura de la Materia, CSIC, E-28006 Madrid, Spain

(Dated: August 19, 2025)

We discuss the Fermi-velocity renormalization in twisted bilayer graphene due to Coulomb exchange interaction within an atomistic tight-binding model. Adopting the Slater-Koster parametrization for the hopping parameters obtained from first principles, our results only depend on the effective dielectric constant  $\epsilon$  and the Hubbard-interaction  $U$ . The Fermi velocity of graphene increases twist-angle independent by 25% for  $\epsilon = 10$  and  $U = 4\text{eV}$ , leading to an increase by more than 100% of the flat bandwidth at twist-angle  $\theta = 1.4^\circ$ . Including also the renormalization of the out-of-plane hopping terms, we further observe a shift of the magic angle from  $1.02^\circ$  to  $0.96^\circ$ . Our results offer a microscopic explanation of the critical temperature,  $T_c$ , as function of the twist angle where the largest  $T_c$  is found at  $\theta_{max} = 1.1^\circ$ . For  $\theta > \theta_{max}$ ,  $T_c$  is obtained from the Bethe-Salpeter equation of the Cooper channel. For  $\theta < \theta_{max}$ , the discussion is based on the critical line of the Berezinskii-Kosterlitz-Thouless phase transition.

**Introduction.** The discovery of superconductivity (SC) in magic-angle twisted bilayer graphene (MATBG) has attracted enormous attention.<sup>1–3</sup> Importantly, SC has also been observed in related multilayer systems with alternating twist angles following the theoretical prediction of Khalaf et al.<sup>4–12</sup> Recently, SC has further been detected in non-commensurable systems such as trilayer graphene with chiral twist.<sup>13–16</sup>

The phase diagram of MATBG shows certain similarity to the one of high- $T_c$  superconductors and the experimental accessibility and tunability of moiré systems fueled the hope to understand the origin of SC in MATBG rather than in cuprates. Nevertheless, even after seven years since the discovery of SC in MATBG, there is still no consensus about the basic pairing mechanism due to the intricate interplay between electronic correlations, topology, strain, and phonons.<sup>17–20</sup>

In this Letter, we will address the twist angle dependence of the critical temperature  $T_c$  of MATBG, recently measured by Cao et al.<sup>21</sup> They obtained a maximal  $T_c$  for a twist angle  $\theta_{max} \approx 1.1^\circ$  and minimal  $T_c$  for  $\theta_{min}^< \approx 0.96^\circ$  and  $\theta_{min}^> \approx 1.2^\circ$ . Crucial for our interpretation of  $T_c(\theta)$  is the renormalization of the Fermi velocity which slows down the approach of the magic-angle condition and explains why the *renormalized* magic-angle condition does not coincide with the maximum of  $T_c$ . This renormalization depends on the effective dielectric environment and we have chosen  $\epsilon = 10$ , close to  $\epsilon = 15$  chosen in Refs. 22–24.

In Fig. 1 (a), the Hartree-Fock renormalized bands at  $\theta = 1.02^\circ$  (dashed black) and at  $\theta = 0.96^\circ$  (full red) are shown. The twist angle  $\theta = 1.02^\circ$  corresponds to the magic angle of the bare bands, however, the band-width of the flat bands is considerable larger than at  $\theta_m^* = 0.96^\circ$  which we identify as the *renormalized* magic angle. This renormalization is caused by the exchange interaction between the flat and the remote bands. The full evolution of the band-structure for different twist-angles can be found in the Supplemental Material (SM).<sup>25</sup>

In the following, we will first present a microscopic ex-

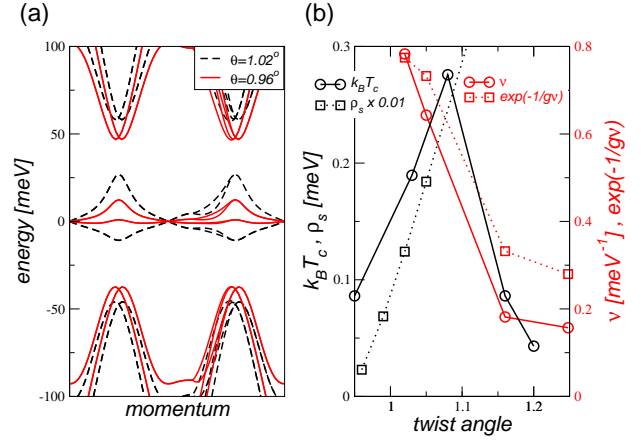


FIG. 1. (a) Hartree-Fock renormalized bands for twist angle  $\theta_m = 1.02^\circ$  (dashed black) which represents the magic angle without exchange interaction and  $\theta_m^* = 0.96^\circ$  (full red) which represents the magic angle including the exchange interaction with  $\epsilon = 10$  and  $U = 4\text{eV}$ . (b) Comparison of the critical temperature  $k_B T_c$  taken from Ref. 21 (black solid circles) and the superfluid stiffness  $\rho_s$  obtained from the Drude weight at optimal doping  $n/n_0 = -2.4$  using the Hartree-Fock renormalized bands (black dashed squares). Also shown is the density of states  $\nu$  at optimal doping (red solid circles) and  $\exp(-1/gv)$  (red dashed squares) with an effective attractive interaction  $g = 5\text{meV}$ .

planation of the twist-angle dependence of  $T_c$ . We will then summarize the results on the Fermi velocity renormalization of single-layer graphene (SLG) and afterwards discuss the Fermi velocity renormalization in twisted bilayer graphene (TBG). Finally, we will give a heuristic formula how to incorporate the effect of the remote bands on the flat band regime.

**Twist-angle dependence of  $T_c$ .** The renormalized magic angle  $\theta_m^*$  roughly coincides with  $\theta_{min}^<$ . The suppression of SC at  $\theta_m^* \approx \theta_{min}^<$  is consistent with the general expect-

tation that the superfluid density is proportional to the band width of the normal state as it can be related to the Drude weight. This is further reflected by the critical line of the Berezinskii-Kosterlitz-Thouless transition given by

$$k_B T_c = \frac{\pi}{2} \rho_s(T_c). \quad (1)$$

Calculating the Drude weight based on the renormalized bands of the normal state at optimal hole doping  $n/n_0 = -2.4$  and then relating the quantity to the superfluid stiffness,<sup>25</sup> we obtain a linear dependence as function of the twist angle for  $\theta > \theta_m^*$ . This is shown as dashed black line in Fig. 1 (b). Also the measured critical temperature is increasing for twist angle with  $\theta_{min}^< \lesssim \theta \lesssim \theta_{max}$ , shown as full black line. However, the experimental  $k_B T_c$  is about a factor 100 smaller than  $\rho_s(T_c)$ , consistent with SC in the phase-fluctuation regime.

To discuss the decay of  $T_c$  for  $\theta_{max} \lesssim \theta \lesssim \theta_{min}^>$ , we start from the Bethe-Salpeter equation of the Cooper channel

$$k_B T_c = \Lambda_B \exp(-1/g\nu), \quad (2)$$

where  $\nu$  denotes the density of states at optimal doping  $n/n_0 = -2.4$ ,  $g$  is an effective attractive contact interaction  $g \sim 5\text{meV}$  and  $\Lambda_B \sim 1\text{meV}$  is a cutoff of the order of the band-width, see SM.<sup>25</sup> As can be seen in Fig. 1 (b), there is suppression of  $T_c$  around  $\theta_{min}^>$  and a saturation of  $T_c$  coming from Eq. (2) for  $\theta \approx \theta_{max}$ . The upper twist angle  $\theta_{min}^>$  can further be related to the appearance of an additional van Hove singularity that triggers Cooper pairing due to additional screening.<sup>26</sup>

To summarize, for larger twist angles  $T_c$  is related to the density of states of the renormalized bands which determines the pairing mechanism. For smaller twist angles,  $T_c$  is related to the Drude weight of the renormalized bands as dictated by the critical line of the Berezinskii-Kosterlitz-Thouless transition. The above interpretation is the first main results of this work.

*Fermi velocity renormalization in SLG.* Fermi velocity renormalization in SLG was theoretically predicted more than 30 years ago by González et al.<sup>27</sup> and subsequently verified by a number of experiments based on measuring the effective cyclotron mass,<sup>28</sup> via scanning tunneling spectroscopy,<sup>29,30</sup> by angle-resolved photoemission spectroscopy,<sup>31</sup> by quantum capacitance measurements,<sup>32</sup> via Landau level spectroscopy,<sup>33</sup> and also indirectly via the Drude weight.<sup>34</sup> Only recently, it was directly observed using the quantum twisting microscope<sup>35</sup> confirming the renormalization of the tunneling matrix element from the bare value  $t \sim 2.7\text{ eV}$  obtained from first-principles to  $t^* \sim 3\text{ eV}$ .

The renormalization of the hopping amplitude or related Fermi velocity can be understood from a one-loop renormalisation group (RG) based on the continuous

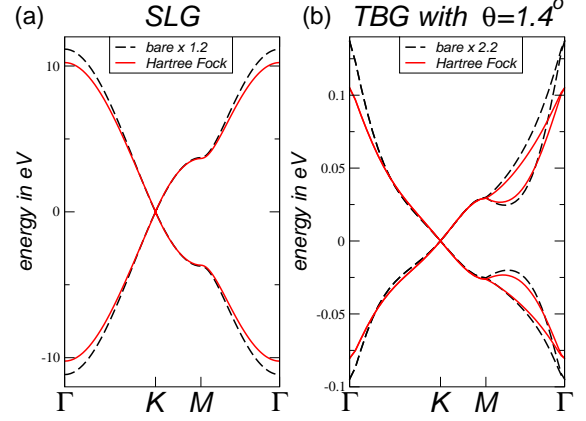


FIG. 2. (a) Dispersion of single-layer graphene without (dashed black) and with (full red) Hartree-Fock renormalization for  $\epsilon = 5$ . The bare band-structure is multiplied by the factor 1.2 amounting to a Fermi velocity renormalization of  $\sim 20\%$ . (b) The flat bands of twisted bilayer graphene at  $\theta = 1.4^\circ$  without (dashed black) and with (full red) Hartree-Fock renormalization for  $\epsilon = 10$  and  $U = 4\text{eV}$ . The bare band-structure is multiplied by the factor 2.2 amounting to a flat band Fermi velocity renormalization of more than  $\sim 100\%$ .

Dirac model<sup>27</sup>

$$\frac{v_F^*}{v_F} = 1 + \frac{\alpha}{4} \ln \frac{\Lambda}{k}, \quad (3)$$

where  $\alpha = \frac{1}{4\pi\epsilon_0\epsilon} \frac{e^2}{\hbar v_F} \approx 2.2/\epsilon$  is the fine-structure constant of graphene with the unrenormalized Fermi velocity  $v_F$  and  $\epsilon$  characterises the static dielectric environment. This formula has been discussed and extended by several authors,<sup>36–48</sup> showing that a self-consistent Hartree-Fock theory remains valid even close to the neutrality point.

In order to make quantitative predictions, a full tight-binding model is needed since only then, ambiguities coming from the cut-off  $\Lambda$  of Eq. (3) can be avoided. In Ref. 49, the cut-off was determined from atomistic tight-binding calculations to be  $\Lambda \sim |\mathbf{K}| = 4\pi/3a$  with  $a = 2.41\text{\AA}$ . Let us further stress that Eq. (3) is only valid in the long-wavelength limit, the full band-structure, however, can well be approximated by scaling the hopping matrix element.<sup>49</sup> For a typical electronic density of  $n = 5 \times 10^{12}\text{cm}^{-2}$ , we obtain from Eq. (3)  $\frac{v_F^*}{v_F} \sim 1.25$ , including internal screening via the modified prefactor  $1/4 \rightarrow 1/[4(1 + (\pi/2)\alpha)]$  and assuming BN-encapsulation with  $\alpha \sim 0.45$ . This estimate is close to the factor 1.2 that is obtained from the full RPA-calculation as shown in Fig. 2 (a).

*Fermi velocity renormalization in TBG.* In TBG, Dirac cones are protected by  $C_2T$ -symmetry<sup>50–57</sup> and the Fermi velocity is strongly reduced compared to SLG for twist angles around the magic angle.<sup>58–61</sup> In order to discuss

the renormalization of the Fermi velocity (or intralayer tunneling) of TBG due to electron-electron interaction without introducing an arbitrary cut-off, we will employ an atomistic tight-binding model and the Coulomb interaction is treated via a self-consistent Hartree-Fock approximation including all bands as outlined in Ref. 62. The final results will only depend on the effective dielectric constant of the long-ranged Coulomb interaction  $\epsilon$  and the regularizing Hubbard interaction  $U$ .

Apart from the renormalization of the intralayer tunneling, there is also the renormalization of the interlayer tunneling. To simplify the discussion, we will mainly focus on the tunneling between  $AA$ -stacked and  $AB$ -stacked regions,  $w_0$  and  $w_1$ .<sup>63</sup> We will also be able to discuss the renormalization of  $\kappa = w_0/w_1$  as function of the twist angle.

Remarkably, the renormalization of both, intra- and interlayer tunneling turns out to be twist-angle independent and leads to a renormalization of the magic angle. This is the second main results of this work and in the following, we will address the technical aspects of our approach. More details can be found in the SM.<sup>25</sup>

*Tight-binding model.* In order to unambiguously discuss the effect of the exchange interaction, we need to start from the non-interacting tight-binding model

$$H_0 = - \sum_{n,m} \sum_{i,j} \sum_{\sigma} t_{n,m}^{i,j} \psi_{n,i,\sigma}^\dagger \psi_{m,j,\sigma}, \quad (4)$$

where the hopping matrix element  $t_{n,m}^{i,j}$  only depends on the vector between the two lattice sites, i.e.,  $t_{n,m}^{i,j} = t(\mathbf{R}_n - \mathbf{R}_m + \boldsymbol{\delta}_i - \boldsymbol{\delta}_j)$  with  $\mathbf{R}_n$  denoting the lattice vector of unit cell  $n$  and  $\boldsymbol{\delta}_i$  the position of lattice site  $i$  with respect to the unit cell. The spin is labeled by  $\sigma$ . We use the Slater-Koster parametrization

$$t(\mathbf{r}) = t_{\parallel} e^{\frac{a_0 - r}{r_0}} \left( 1 - \left( \frac{\mathbf{r} \cdot \mathbf{e}_z}{r} \right)^2 \right) + t_{\perp} e^{\frac{d_{\perp} - r}{r_0}} \left( \frac{\mathbf{r} \cdot \mathbf{e}_z}{r} \right)^2,$$

where  $a_0 = 1.42\text{\AA}$  is the C-C distance,  $r_0 = 0.319a_0$  the decay parameter, and  $d_{\perp} = 3.34\text{\AA}$  denotes the interlayer distance. We further set  $t_{\parallel} = 2.7\text{eV}$  and  $t_{\perp} = -0.48\text{eV}$ .<sup>64</sup>

*Coulomb interaction.* The total Hamiltonian shall be written as  $H = H_0 + H_{\text{int}}$  where the interaction term is split into a long-ranged Coulomb interaction and a short-ranged on-site Hubbard term,  $H_{\text{int}} = H_V + H_U$ , with

$$H_V = \frac{1}{2} \sum_{n,m} \sum_{i,j} \sum_{\sigma,\sigma'} V_{n,m}^{i,j} \psi_{n,i,\sigma}^\dagger \psi_{m,j,\sigma'}^\dagger \psi_{m,j,\sigma'} \psi_{n,i,\sigma}, \quad (5)$$

$$H_U = \frac{U}{2} \sum_{n,i} \sum_{\sigma} \psi_{n,i,\sigma}^\dagger \psi_{n,i,\bar{\sigma}}^\dagger \psi_{n,i,\bar{\sigma}} \psi_{n,i,\sigma}, \quad (6)$$

where  $\bar{\sigma}$  denotes the opposite spin-projection. The Coulomb potential only depends on the distance between the two lattice sites,  $V_{n,m}^{i,j} = v(|\mathbf{R}_n - \mathbf{R}_m + \boldsymbol{\delta}_i - \boldsymbol{\delta}_j|)$ , and is implemented by the double-gated potential<sup>65</sup>

$$v(|\mathbf{r}|) = \frac{e^2}{4\pi\epsilon_0\epsilon} \sum_n \frac{(-1)^n}{|\mathbf{r} + n\xi\mathbf{z}|} \xrightarrow{r \gg \xi} \frac{e^2}{4\pi\epsilon_0\epsilon} \frac{2\sqrt{2}e^{-\pi r/\xi}}{\xi\sqrt{r/\xi}},$$

where  $\epsilon$  stands for the intrinsic effective dielectric constant of the system. We will further choose  $\xi = 10\text{nm}$ .<sup>3,66</sup>

The Fermi-velocity renormalization is now discussed within the self-consistent Hartree-Fock approximation which obeys all crystallographic and valley symmetries following Ref. 62, see also SM.<sup>25</sup> At the neutrality point, the Dirac-cones are thus preserved with a renormalized "flat band" Fermi velocity which shall not be confused with the renormalized Fermi velocity of Eq (11).

*Mapping to the BM model.* The seminal Bistritzer-MacDonald model<sup>61</sup> for MATBG is written in the basis of plane wave basis  $\{|\mathbf{k}, \sigma, \ell\rangle\}$ . Focusing on the  $K$ -valley, the intralayer Hamiltonian reads

$$\langle \mathbf{k}, \ell | H | \mathbf{k}, \ell \rangle = \hbar v_F (k_x^\ell \sigma_x - k_y^\ell \sigma_y), \quad (7)$$

with  $\langle \mathbf{k}, \ell | H | \mathbf{k}, \ell \rangle$  a matrix in sublattice space,  $\sigma_i$  the identity ( $i = 0$ ) and Pauli ( $i = x, y, z$ ) matrices and  $\mathbf{k}^\ell = R_{-\ell\theta/2}(\mathbf{k})$  the rotated momentum. The interlayer Hamiltonian couples plane waves with momentum exchange  $\mathbf{q}_1 = \mathbf{K}_b - \mathbf{K}_t$ ,  $\mathbf{q}_2 = R_{2\pi/3}(\mathbf{q}_1)$  and  $\mathbf{q}_3 = R_{-2\pi/3}(\mathbf{q}_1)$ ,

$$\langle \mathbf{k} + \mathbf{q}_n, t | H | \mathbf{k}, b \rangle = w_0^n + w_1^n \sigma_x + w_2^n \sigma_y, \quad (8)$$

with  $w_0^n = w_0^1$ ,  $w_1^n = \cos(2\pi(n-1)/3)w_1^1$ , and  $w_2^n = -\sin(2\pi(n-1)/3)w_2^1$ , which can be written as a function of  $w_i \equiv w_i^1$ .

For the rigid lattice without relaxation, the BM model is accurate only for larger twist angles. For twist angles close to the magic angle, lattice relaxation needs to be implemented via the coupling to a pseudo-gauge field  $\mathbf{A}$ , with Fourier components  $\mathbf{A}(\mathbf{g})$ , in the intralayer Hamiltonian,<sup>67-71</sup>

$$\langle \mathbf{k} + \mathbf{g}, \ell | H | \mathbf{k}, \ell \rangle = \gamma v_F (A_x^\ell(\mathbf{g}) \sigma_x - A_y^\ell(\mathbf{g}) \sigma_y), \quad (9)$$

with  $\mathbf{A}^\ell(\mathbf{g}) = \ell R_{\ell\theta/2}(\mathbf{A}(\mathbf{g}))$ . In this work, we will use a different notation, namely

$$\langle \mathbf{k} + \mathbf{g}, \ell | H | \mathbf{k}, \ell \rangle = \gamma_1^\ell(\mathbf{g}) \sigma_x + \gamma_2^\ell(\mathbf{g}) \sigma_y. \quad (10)$$

Let us finally mention that in order to accurately describe the atomistic band structures, a more complex theory is needed. Additional contributions include terms quadratic in momentum in the intralayer Hamiltonian<sup>71</sup> and a dependence of  $v_F^*$  on  $|\mathbf{k}|$  similar to Eq. (3), momentum dependence,<sup>70,71</sup> and terms with larger momentum exchange in the interlayer couplings,<sup>70-72</sup> as well as new interlayer coupling terms proportional to  $i\sigma_z$ .<sup>69,71</sup>

*Main results.* The main effect of the mean-field renormalization is the enhancement of the Fermi velocity of SLG, which is basically unaffected by the moiré lattice and thus independent of the twist angle. In Fig. 3 (a), the linear dependence of the matrix element  $\langle \mathbf{K}_b + \mathbf{k}, A, b | H | \mathbf{K}_b + \mathbf{k}, B, b \rangle$  as function of  $|\mathbf{k}|$  in different directions is shown for  $\theta = 0.96^\circ$ .

Interlayer couplings with nonzero momentum exchange also renormalize in the normal state, see Fig. 3 (b). We

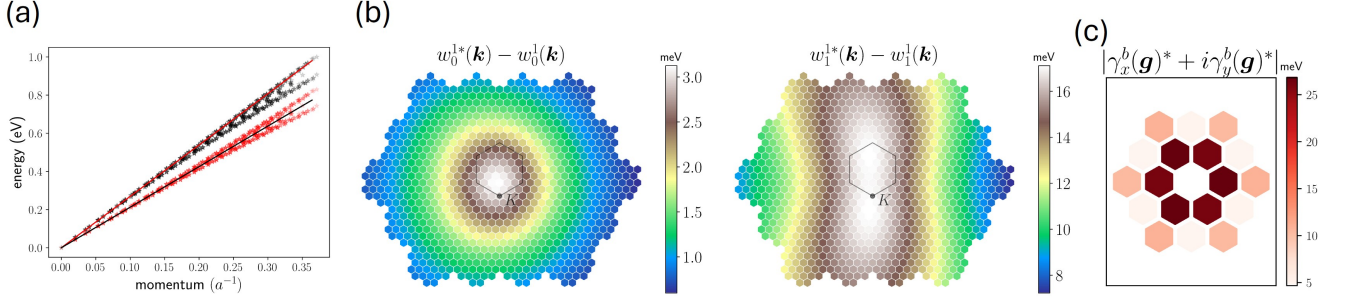


FIG. 3. (a) Intralayer Hamiltonian matrix element  $\langle \mathbf{K}_b + \mathbf{k}, A, b | H | \mathbf{K}_b + \mathbf{k}, B, b \rangle$  as function of  $|\mathbf{k}|$  in different directions. The overall linear trend comes from the Fermi velocity, and the spread comes from a subdominant quadratic component that depends on the angle. Black and red stars stand for the renormalized and bare systems, respectively. There is a slight bending in the renormalized data that comes from logarithmic corrections, see Eq. (3). (b) Interlayer couplings,  $w_{0,1}^1(\mathbf{k})$ , after subtracting the non interacting part  $w_{0,1}^1(\mathbf{k})$ . The 1st Brillouin zone is indicated by a black line, also indicating the  $K$ -point and is composed of 36 smaller hexagons. Note that  $w_0^{1*}$  and  $w_1^{1*}$  show different  $\mathbf{k}$  dependence. (c) Intralayer couplings for several exchange momenta  $\mathbf{g}$ . The first shell of these momenta compose the dominant couplings.

get the following values at  $\mathbf{k} = 0$ :

$$v_F^* = 2.692 \text{ eV} \times a, \quad v_F = 2.125 \text{ eV} \times a \quad (11)$$

$$w_0^* = 55.4 \text{ meV}, \quad w_0 = 58.4 \text{ meV} \quad (12)$$

$$w_1^* = 142.3 \text{ meV}, \quad w_1 = 125.3 \text{ meV} \quad (13)$$

For the  $\gamma$  couplings with momentum  $\mathbf{g}_1, \mathbf{g}_2$  of the bottom layer, we get

$$\begin{aligned} \gamma_1^b(\mathbf{g}_1)^* &= -22.1 \text{ meV}, & \gamma_1^b(\mathbf{g}_1) &= -19.6 \text{ meV} \\ \gamma_2^b(\mathbf{g}_1)^* &= -13.7 \text{ meV}, & \gamma_2^b(\mathbf{g}_1) &= -11.5 \text{ meV} \\ \gamma_1^b(\mathbf{g}_2)^* &= 23.2 \text{ meV}, & \gamma_1^b(\mathbf{g}_2) &= 20.3 \text{ meV} \\ \gamma_2^b(\mathbf{g}_2)^* &= -13.4 \text{ meV}, & \gamma_2^b(\mathbf{g}_2) &= -11.5 \text{ meV}. \end{aligned}$$

Values for momenta  $\mathbf{g}_2 - \mathbf{g}_1, -\mathbf{g}_1, -\mathbf{g}_2$  and  $\mathbf{g}_1 - \mathbf{g}_2$ , as well as for the top layer can be obtained from symmetry, see SM.<sup>25</sup> In Fig. 3 (c), the intralayer couplings for several exchange momenta  $\mathbf{g}$  are shown.

In the above equations, we have reported the values of the couplings at  $\mathbf{k} = 0$ . However, an accurate description of MATBG adds a momentum dependence to the couplings,  $w_i^n \rightarrow w_i^n(\mathbf{k})$  and  $\gamma^\ell(\mathbf{g}) \rightarrow \gamma_i^\ell(\mathbf{g}, \mathbf{k})$ . In the non-interacting system, they can be well approximated by linear functions of  $\mathbf{k}$ .<sup>70,71</sup> This can be traced back to the fact that the hopping function is short-ranged. In the Hartree-Fock state, however, the exchange interaction induces arbitrary long-ranged hoppings and the couplings become rather complicated functions of  $\mathbf{k}$ , see Fig 3 (b).

*Effective BM model.* TBG can be well described by the BM model where only the three parameters  $v_F, w_0, w_1$  and the twist angle  $\theta$  enter. Setting the moiré length to 1, the model can be further simplified to only depend on two dimensionless quantities  $\alpha_i = w_i/v_F k_\theta$ , where  $k_\theta = 2|\mathbf{K}| \sin \theta/2$  with  $|\mathbf{K}| = 4\pi/3a$ . Perturbation theory then yields the "effective" Fermi velocity of the flat band as  $v_F^{fb}/v_F = (1 - 3\alpha_1^2)/(1 + 3(\alpha_0^2 + \alpha_1^2))$ . The magic angle is thus defined by  $\alpha_1^2 = 1/3$  and using the parameters of Ref. 61 with  $w_1 = 110\text{meV}$  and  $v_F = 2.408 \text{ eV} \times a$ , one

obtains  $\theta_m = 1.08^\circ$ . Notice that these parameters are quite different from Eqs. (13) and (11), indicating that more parameters are needed for an accurate mapping of the BM to the tight-binding model, see also SM.<sup>25</sup>

The effective BM model including the exchange interaction between the flat and remote bands can be obtained by defining the renormalized parameters  $\alpha_i^* = \zeta_i \alpha_i$  with  $\zeta_0 = 0.749$  and  $\zeta_1 = 0.896$ , see Eqs. (11) - (13). This yields the renormalized magic angle  $\theta_m^* = \zeta_1 \theta_m = 0.97^\circ$ , close to what is obtained from the renormalized bands of Fig. 1 (a).

Let us also discuss  $\kappa = w_0/w_1$ , first approximated to be  $\kappa \approx 0.817$ .<sup>63</sup> For the non-interacting model, our projection method yields  $\kappa = 0.466$ . For the interacting model, we have  $\kappa^* = 0.389$  tending even further to the chiral limit as first discussed by Vafeek and Kang.<sup>73</sup>

We can also estimate the renormalized flat band Fermi velocity which does depend on the twist angle. Using the perturbative formula yields

$$\frac{v_F^{fb*}}{v_F^{fb}} = \frac{(1 - 3\alpha_1^2 \zeta_1^2)(1 + 3\alpha_1^2[1 + \kappa^2])}{(1 - 3\alpha_1^2)(1 + 3\alpha_1^2 \zeta_1^2[1 + (\kappa^*)^2])}. \quad (14)$$

With the parameters of the BM model, this gives a renormalization factor of 1.5 for  $\theta = 1.4^\circ$ . For slightly different parameters with  $w_1 = 125\text{meV}$  and  $v_F = 2.233 \text{ eV} \times a$ , one obtains  $v_F^{fb*}/v_F^{fb} = 2.2$ , see also SM.<sup>25</sup> Scaling the bare bands by this factor yields good agreement with the renormalized bands not only around the  $K$ -point, but throughout the Brillouin zone similar to SLG, as shown in Fig. 2 (b).

*Conclusions.* Using the approach outlined in Ref. 62, we have analyzed the renormalization of the electronic bands of TBG due to the exchange interaction between the flat and remote bands. This renormalization depends on the dielectric environment, but always amounts to a down-shift of the magic angle.

The effect of the exchange interaction can be well captured by renormalizing the inplane Fermi velocity and the

interplane hopping elements  $w_0$  and  $w_1$  which turn out to be twist-angle independent. The renormalized flat bands for larger twist angles can further be well approximated by simply scaling the bare flat bands by a twist-angle dependent factor.

The renormalization of the magic angle in MATBG should be taken into account for the proper interpretation of experimental results with reduced screening. The twist angle dependence of the critical temperature, e.g., can be explained by one-particle quantities such as the Drude weight and the density of states, invoking the

Berezinskii-Kosterlitz-Thouless transition and the Bethe-Salpeter equation of the Cooper channel, respectively.

*Acknowledgement.* We thank Patrick Ledwith, Eslam Khalaf, and Suheng Xu for useful discussions. The work was supported by grant PID2023-146461NB-I00 funded by Ministerio de Ciencia, Innovación y Universidades as well as by the CSIC Research Platform on Quantum Technologies PTI-001 and the Severo Ochoa Centres of Excellence program through Grant CEX2024-001445-S. The access to computational resources of CESGA (Centro de Supercomputación de Galicia) is also gratefully acknowledged.

## Supplemental Material

### I. BAND-STRUCTURE OF TBG AND COMPARISON TO THE CONTINUUM MODEL

The renormalization of the magic angle can be seen directly from the band-structure of the tight-binding model as function of the commensurate twist angles  $\cos\theta = 1 - 0.5/A_i$  with  $A_i = 3i^2 + 3i + 1$  for a fixed dielectric environment  $\epsilon_r = 10$  and Hubbard-interaction  $U = 4\text{eV}$ . In Fig. 4, we show the flat and first remote bands as black curves and the smallest band-width is obtained for  $\theta = 0.96^\circ$ , corresponding to  $i = 34$ . Moreover, by considering the irreducible representations of the upper two and lower two degenerate bands at the  $\Gamma$ -point,<sup>70</sup> one sees that the upper (lower) two flat bands transform as  $A_2 + B_2$  ( $A_1 + B_1$ ) of the  $D_6$  point group for  $\theta < 0.96^\circ$ , whereas it is swapped for  $\theta > 0.96^\circ$ .

The swap of irreducible representations is also seen in the bare band-structure, however, at the unrenormalized magic angle  $i = 32$ . This means that even though the bands for  $\theta = 1.05^\circ$  and  $\theta = 0.99^\circ$  appear similar, analyzing their transformation properties at the  $\Gamma$ -point reveals a band-crossing and thus a magic angle at  $\theta \approx 1.02^\circ$  ( $i = 32$ ).

Let us also discuss the band-structure of the continuum model with the parameters that were obtained from the procedure described in the main text and below. Including the parameters related to the first shell of the interlayer coupling already yields a good approximation of the remote bands. The band-width of the flat bands, however, turns out to be considerably smaller as can be seen in Fig. 5. Including additionally the first shell of the intra-layer couplings yields almost perfect agreement with the full renormalized band-structure of the underlying tight-binding model, validating our approach.

Let us now only include the parameters of the zeroth shell yielding the original BM model. As discussed in the main text, this yields an expression for the renormalized

flat-band Fermi velocity

$$\frac{v_F^{fb*}}{v_F^{fb}} = \frac{(1 - 3\alpha_1^2\zeta_1^2)(1 + 3\alpha_1^2[1 + \kappa^2])}{(1 - 3\alpha_1^2)(1 + 3\alpha_1^2\zeta_1^2[1 + (\kappa^*)^2])}, \quad (15)$$

with  $\alpha_1 = w_1/v_F k_\theta$ , where  $k_\theta = 2|\mathbf{K}| \sin\theta/2$  with  $|\mathbf{K}| = 4\pi/3a$ . We further have  $\kappa = 0.466$ ,  $\kappa^* = 0.389$ , and  $\zeta_i = 0.896$ . For the BM model, we now set  $w_1 = 110\text{meV}$  and  $v_F = 2.408 \text{ eV} \times a$ , whereas an alternative parameter choice is  $w_1 = 125\text{meV}$  and  $v_F = 2.330 \text{ eV} \times a$  which yields the correct factor for the twist angle  $\theta = 1.4^\circ$ .

In Fig. 6, we show the renormalized flat band Fermi velocity as function of the twist angle for the two parameter sets. Obviously, Eq. (15) breaks down for twist angles close to the magic angle.

### II. VALLEY SYMMETRY IN THE TIGHT-BINDING MODEL

Our self-consistent algorithm seeks a renormalized state that preserves all symmetries of the system. Even if time-reversal and crystallographic symmetries are conserved by construction, one can still converge towards an intervalley coherent state that breaks the valley charge conservation. The valley charge, however, is an emergent quantity that is not unambiguously defined in the atomistic setup. Here, we describe our method to preserve the valley symmetry within the tight-binding model.

Our self-consistent algorithm is based on the Fock matrix  $\langle\psi_{\mathbf{r}}^\dagger\psi_{\mathbf{r}'}\rangle$ , where  $\psi_{\mathbf{r}}^\dagger$  ( $\psi_{\mathbf{r}}^\dagger$ ) annihilates (creates) an electron at site  $\mathbf{r}$  and for conciseness, we omit the spin in this discussion. The position vectors  $\mathbf{r}$ ,  $\mathbf{r}'$  are limited to the first moiré unit cell, denoted by  $\delta_i$ ,  $\delta_j$  in the main text.

The Fock matrix can be written as a sum over the occupied Bloch states,  $\{|\mathbf{k}n\rangle\}$ , with  $n = \dots -1, 1, \dots$  the band index that is a positive number for conduction states, and negative for valence states (the 4 flat bands then



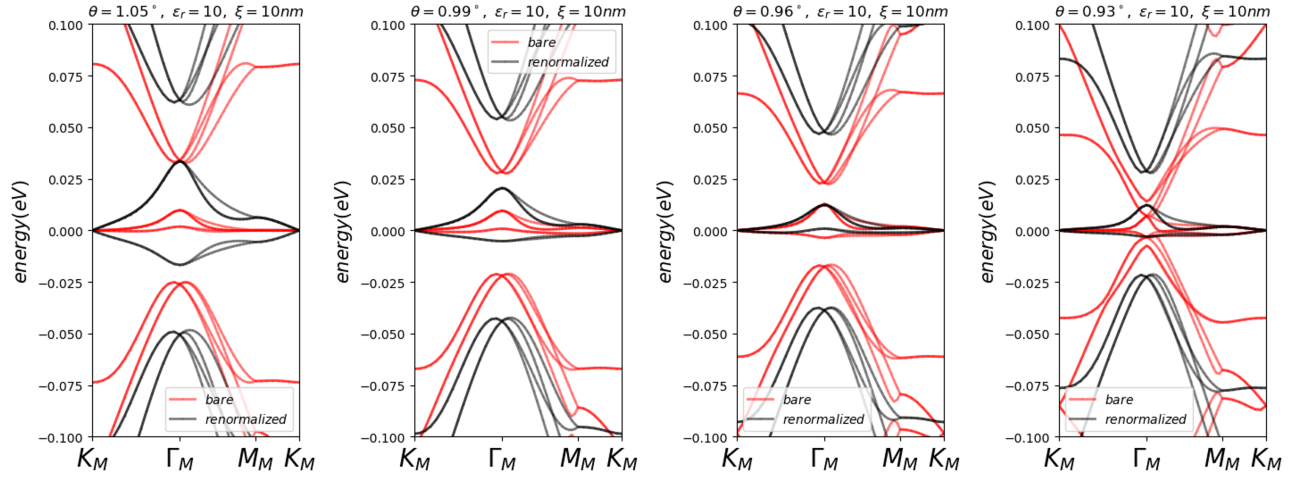


FIG. 4. Band-structure for various commensurate twist angles  $\cos \theta = 1 - 0.5/A_i$  with  $A_i = 3i^2 + 3i + 1$  of the bare (red curves) and renormalized (black) tight-binding Hamiltonian. The renormalized magic angle is given by  $\theta = 0.96^\circ$  ( $i = 34$ ), whereas the bare magic angle turns out to be  $\theta = 1.02^\circ$  ( $i = 32$ ) (not shown above). Note that the irreducible representations of the two degenerate flat bands at the  $\Gamma$ -point are inverted for  $i = 33$  and  $i = 35$  (renormalized bands) respectively  $i = 31$  and  $i = 33$  (bare bands).

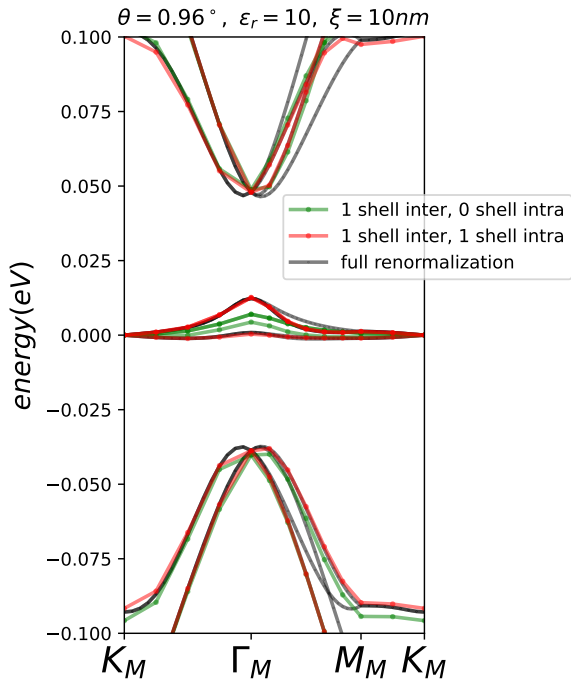


FIG. 5. Band-structure for two different plane-wave continuum Hamiltonians compared to the bands of the fully renormalized Hamiltonian of the underlying tight-binding model.

correspond to  $n = -2, -1, 1, 2$ ). We thus get

$$\langle \psi_{\mathbf{r}}^\dagger \psi_{\mathbf{r}'} \rangle = \sum_{\varepsilon_{\mathbf{k}n} < \varepsilon_F} \langle \mathbf{r}' | \mathbf{k}n \rangle \langle \mathbf{k}n | \mathbf{r} \rangle, \quad (16)$$

where the sum is restricted to occupied states.

We proceed by distinguishing the central 20 bands,<sup>62</sup>

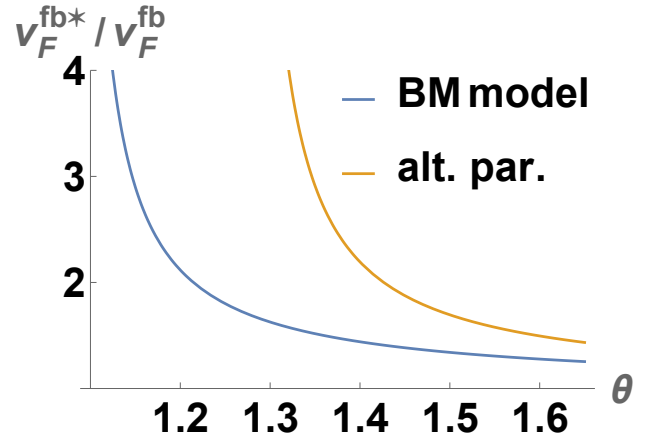


FIG. 6. Renormalization of the flat band Fermi velocity as function of the twist angle for parameters of the BM model (blue curve) and the alternative parameter set (beige curve).

i.e., the first 10 valence and conduction bands, and write

$$\langle \psi_{\mathbf{r}}^\dagger \psi_{\mathbf{r}'} \rangle = \sum_{n < -10} \langle \mathbf{r}' | \mathbf{k}n \rangle \langle \mathbf{k}n | \mathbf{r} \rangle + \sum_{\substack{n \geq -10 \\ \varepsilon_{\mathbf{k}n} < \varepsilon_F}} \langle \mathbf{r}' | \mathbf{k}n \rangle \langle \mathbf{k}n | \mathbf{r} \rangle. \quad (17)$$

We now project the microscopic valley operator  $\tilde{\tau}_z$ , defined, e.g., in Ref. 62, for each momentum onto the central 20 bands, with  $n, m = -10, \dots, 10$ :

$$[\tilde{\tau}_z(\mathbf{k})]_{nm} = \langle \mathbf{k}n | \tilde{\tau}_z | \mathbf{k}m \rangle \quad (18)$$

The eigenvalues of  $\tilde{\tau}_z(\mathbf{k})$  are typically of the order of  $\pm 0.99$  and we can introduce the unitary matrix  $\tau_z(\mathbf{k}) = \tilde{\tau}_z(\mathbf{k}) / \sqrt{\tilde{\tau}_z(\mathbf{k})^2}$  with eigenvalue 1(−1) for the states in

valley  $K(K')$ . By this, we have defined the valley charge with respect to the central 20 bands. Notice that the subspace of the central bands changes after each self-consistency loop, hence, we define a slightly different  $\tau_z(\mathbf{k})$  for each iteration. Finally, we get the valley-

transformed Bloch functions,

$$|\mathbf{k}n\rangle_{\tau_z} = [\tau_z(\mathbf{k})]_{nm} |\mathbf{k}m\rangle. \quad (19)$$

The valley symmetry is now enforced via the modified Fock matrix

$$\langle \psi_{\mathbf{r}}^\dagger \psi_{\mathbf{r}'} \rangle \rightarrow \sum_{n < -10} \langle \mathbf{r}' | \mathbf{k}n \rangle \langle \mathbf{k}n | \mathbf{r} \rangle + \frac{1}{2} \sum_{\substack{n \geq -10 \\ \varepsilon_{\mathbf{k}n} < \varepsilon_F}} \langle \mathbf{r}' | \mathbf{k}n \rangle \langle \mathbf{k}n | \mathbf{r} \rangle + \frac{1}{2} \sum_{\substack{n \geq -10 \\ \varepsilon_{\mathbf{k}n} < \varepsilon_F}} \langle \mathbf{r}' | \mathbf{k}n \rangle_{\tau_z \tau_z} \langle \mathbf{k}n | \mathbf{r} \rangle, \quad (20)$$

which is fed into the algorithm.

We have checked that the converged solutions are fixed points of the Hartree-Fock theory also without explicitly enforcing the valley symmetry, validating our method. With this procedure we arrive at a valley-preserving solution, avoiding the intervalley coherent phase with lower energy, especially at the renormalized magic angle.

### III. TRUNCATED ATOMIC PLANE WAVES

The low-energy states can be expressed in terms of the atomic plane waves<sup>72,74</sup>

$$\langle \mathbf{r} | \mathbf{k}, \tau, \sigma, \ell \rangle = \frac{2}{\sqrt{N_c N_{at}}} e^{i(\tau \mathbf{K}_\ell + \mathbf{k}) \cdot \mathbf{r}_{nr}} \delta_{\mathbf{r} \in \{\sigma \ell\}}, \quad (21)$$

where  $\tau = \pm$  denotes the valley and  $\mathbf{K}_\ell$  is the  $K$ -point of layer  $\ell$ ,  $\mathbf{K}_\ell = R(\theta/2)\mathbf{K}$  for  $\ell = \text{top}$  and  $R(-\theta/2)\mathbf{K}$  for  $\ell = \text{bottom}$ , i.e.,  $R$  denotes the  $2 \times 2$  rotation matrix.

The Kronecker delta in Eq. (21) indicates that the plane waves are projected onto layer  $\ell$  and sublattice  $\sigma = A, B$ . Furthermore,  $\mathbf{r}_{nr}$  denotes the atomic positions of the rigid lattice without atomic relaxation,  $N_{at}$  is the number of atoms in the unit cell, i.e., for each sublattice and layer, there are  $N_{at}/4$  atoms in the unit cell, and  $N_c = N_k \times N_k$  is the number of unit cells in the (periodic) system. The set of plane waves is orthonormal with  $\mathbf{k} \cdot \mathbf{g}_{1,2} = 2\pi\mathbb{Z}/N_k$ .

In TBG, the two valleys are decoupled, hence, we can focus on valley  $K$  and will drop the valley index. The opposite valley  $K'$  is recovered by a spinless time-reversal transformation of valley  $K$ .

The plane waves couple according to the moiré periodicity, i.e., the momenta  $\mathbf{k}$  couple to  $\mathbf{k} + \mathbf{g}$  of the same layer, whereas momenta  $\mathbf{K}_t + \mathbf{k}$  of the top layer couple to  $\mathbf{K}_b + \mathbf{k} + \mathbf{g}$  of the bottom layers, with  $\mathbf{g}$  a moiré reciprocal vector. Notice that the mismatch of momentum origin for different layers in Eq. (21) introduces the momentum  $\mathbf{q}_1 = \mathbf{K}_b - \mathbf{K}_t$  in the moiré scattering condition. The Brillouin zone of the original graphene layers then gets folded onto the moiré Brillouin zone spanned by  $\mathbf{g}_1$  and  $\mathbf{g}_2$ .

Let us now discuss the symmetry properties of inter-layer scattering processes, in particular the first shell of momentum exchange, i.e.,  $\mathbf{q}_1, \mathbf{q}_2 = R_{2\pi/3}(\mathbf{q}_1), \mathbf{q}_3 = R_{-2\pi/3}(\mathbf{q}_1)$ .  $C_{2z}\mathcal{T}$  symmetry acts as  $\sigma_x \mathcal{K}$  with  $\mathcal{K}$  the complex conjugation, and is local in momentum space. It constrains the matrix elements,

$$\langle \mathbf{k} + \mathbf{q}_n, t | \mathcal{H} | \mathbf{k}, b \rangle = w_0^n(\mathbf{k}) + w_1^n(\mathbf{k})\sigma_x + w_2^n(\mathbf{k})\sigma_y + iw_3^n(\mathbf{k})\sigma_z, \quad (22)$$

with real functions  $w_{0,1,2,3}^n(\mathbf{k})$ .  $C_{2x}$  symmetry, sending  $\mathbf{k} = (k_x, k_y) \rightarrow M_x(\mathbf{k}) = (k_x, -k_y)$  and acting as  $\sigma_x \mu_x$  with  $\mu_x$  the  $x$ -component of the Pauli matrix with respect to the layer index, imposes the constraints

$$\begin{aligned} w_0^1(\mathbf{k}) &= w_0^1(M_x(\mathbf{k})), \\ w_1^1(\mathbf{k}) &= w_1^1(M_x(\mathbf{k})), \\ w_2^1(\mathbf{k}) &= -w_2^1(M_x(\mathbf{k})), \\ w_3^1(\mathbf{k}) &= w_3^1(M_x(\mathbf{k})). \end{aligned} \quad (23)$$

The  $C_{3z}$  symmetry, sending  $\mathbf{k} \rightarrow R_{2\pi/3}(\mathbf{k})$  and acting as  $e^{-2\pi i/3} \sigma_z$ , relates the different momenta  $\mathbf{q}_i$  as follows:

$$\begin{aligned} w_{0,3}^n(\mathbf{k}) &= w_{0,3}^1(R_{2\pi(n-1)/3}(\mathbf{k})), \\ w_1^n(\mathbf{k}) &= \cos\left(\frac{2\pi(n-1)}{3}\right) w_1^1(R_{2\pi(n-1)/3}(\mathbf{k})) \\ &\quad + \sin\left(\frac{2\pi(n-1)}{3}\right) w_2^1(R_{2\pi(n-1)/3}(\mathbf{k})), \\ w_2^n(\mathbf{k}) &= \cos\left(\frac{2\pi(n-1)}{3}\right) w_2^1(R_{2\pi(n-1)/3}(\mathbf{k})) \\ &\quad - \sin\left(\frac{2\pi(n-1)}{3}\right) w_1^1(R_{2\pi(n-1)/3}(\mathbf{k})) \end{aligned} \quad (24)$$

In the BM model and in the main text, we consider the simplest case of momentum-independent matrix elements. Moreover,  $w_3^n$  is subdominant and taken to zero. Then, by Eq. (23),  $w_2^n = 0$  and we are left with  $w_0 \equiv w_0^1$  and  $w_1 \equiv w_1^1$ . In the original BM model,  $w_0 = w_1$ , appropriate for the unrelaxed lattice; lattice relaxation leads to  $w_0 < w_1$ .<sup>63,69,71</sup>

Let us now consider the intralayer couplings with finite momentum exchange, in particular the first shell of

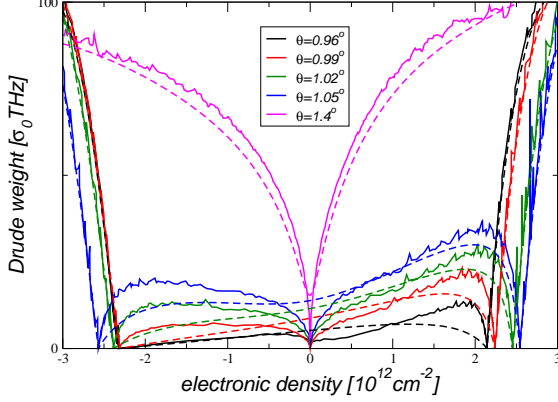


FIG. 7. The Drude weight for various twist angles at  $T = 0$  (solid lines) and at  $T = 40K$  (dashed lines).

momenta,  $\pm \mathbf{g}_1, \pm \mathbf{g}_2, \pm \mathbf{g}_2 - \mathbf{g}_1$ . Again, by  $C_{2z}\mathcal{T}$ , we can write

$$\langle \mathbf{k} + \mathbf{g}, \ell | \mathcal{H} | \mathbf{k}, \ell \rangle = \gamma_0^\ell(\mathbf{g}, \mathbf{k}) + \gamma_1^\ell(\mathbf{g}, \mathbf{k})\sigma_x + \gamma_2^\ell(\mathbf{g}, \mathbf{k})\sigma_y + i\gamma_3^\ell(\mathbf{g}, \mathbf{k})\sigma_z, \quad (25)$$

with real coefficients  $\gamma_i^\ell(\mathbf{g}, \mathbf{k})$ .  $C_{2x}$  symmetry relates the components of different layers,

$$\begin{aligned} \gamma_{0,1}^\ell(\mathbf{g}, \mathbf{k}) &= \gamma_{0,1}^{\bar{\ell}}(M_x(\mathbf{g}), M_x(\mathbf{k})), \\ \gamma_{2,3}^\ell(\mathbf{g}, \mathbf{k}) &= -\gamma_{2,3}^{\bar{\ell}}(M_x(\mathbf{g}), M_x(\mathbf{k})), \end{aligned} \quad (26)$$

with  $\bar{\ell}$  the layer opposite to  $\ell$ ; we can then focus on the bottom layer.  $C_{3z}$  imposes the following constraints:

$$\begin{aligned} \gamma_{0,3}^b(\mathbf{g}_{sn}, \mathbf{k}) &= \gamma_{0,3}^b(\mathbf{g}_n, R_{2\pi s/3}(\mathbf{k})), \\ \gamma_1^b(\mathbf{g}_{sn}, \mathbf{k}) &= \cos\left(\frac{2\pi s}{3}\right) \gamma_1^b(\mathbf{g}_n, R_{2\pi s/3}(\mathbf{k})) \\ &\quad + \sin\left(\frac{2\pi s}{3}\right) \gamma_2^b(\mathbf{g}_n, R_{2\pi s/3}(\mathbf{k})), \\ \gamma_2^b(\mathbf{g}_{sn}, \mathbf{k}) &= \cos\left(\frac{2\pi s}{3}\right) \gamma_2^b(\mathbf{g}_n, R_{2\pi s/3}(\mathbf{k})) \\ &\quad - \sin\left(\frac{2\pi s}{3}\right) \gamma_1^b(\mathbf{g}_n, R_{2\pi s/3}(\mathbf{k})), \end{aligned} \quad (27)$$

where  $n = 1, 2$  and  $s = \pm$ , with  $\mathbf{g}_{+1} = \mathbf{g}_2 - \mathbf{g}_1$ ,  $\mathbf{g}_{-1} = -\mathbf{g}_2$ ,  $\mathbf{g}_{+2} = -\mathbf{g}_1$  and  $\mathbf{g}_{-2} = \mathbf{g}_1 - \mathbf{g}_2$ . Hence, only  $\gamma_i^b(\mathbf{g}_1, \mathbf{k})$  and  $\gamma_i^b(\mathbf{g}_2, \mathbf{k})$  are independent.

In the main text, we report the values at the  $K$ -point, i.e., at  $\mathbf{k} = 0$ , of the dominant couplings,  $\gamma_1^b(\mathbf{g}_{1,2})$  and  $\gamma_2^b(\mathbf{g}_{1,2})$ . These approximations amount to taking the first shell of momentum components of the pseudo-vector potential,<sup>67–70</sup> induced by the lattice relaxation in the non-interacting limit and renormalized in the mean-field state.

#### IV. SUPERFLUID STIFFNESS AND DRUDE WEIGHT

A convenient quantity to characterize the superconducting state is the Drude weight as it can be related to the superfluid stiffness. The Drude weight is a band-structure property and characterized by the velocity in the, say,  $x$ -direction at the Fermi surface. Quasi-flat bands, therefore, necessarily lead to a small Drude weight and consequentially to a suppression of superconductivity. We thus do not expect a maximal critical temperature at the renormalized magic angle in TBG.

We will calculate the Drude weight at the chemical potential  $\mu$  using the following formula:

$$D(\mu) = \left(\frac{e}{\hbar}\right)^2 \frac{g_s}{A} \sum_{\mathbf{k}, n} |v_{\mathbf{k}, n}^x|^2 \partial_\mu f(\epsilon_{\mathbf{k}, n} - \mu), \quad (28)$$

with  $g_s = 2$  denoting the spin-degeneracy,  $A = N_c A_m$  the sample area with  $A_m$  the area of the moiré unit cell, and  $f$  the Fermi function. The velocity vertex  $\hbar v^x = \partial H / \partial k_x$  is defined with respect to the Hartree-Fock Hamiltonian. The superfluid stiffness is then related to the Drude weight by

$$\rho_s = \left(\frac{\hbar}{e}\right)^2 D. \quad (29)$$

The self-consistent calculations use periodic boundary conditions with  $N_c = 36$ . The Drude weights, however, are calculated with  $N_c = 900$ . Even though the Brillouin zone around the magic angle is rather small, there is still noise at  $T = 0$  due to the finite grid.

There is little temperature dependence of the Drude weight for low temperatures  $T \lesssim 5K$ . However, there is a considerable temperature dependence of  $D$  for larger temperatures  $T \sim 40K$  as seen from the dashed curves of Fig. 7. Nevertheless, there is again an approximate proportionality of  $D$  at  $n/n_0 = -2.4$  as function of the twist angle as dictated by the Berezinskii-Kosterlitz-Thouless transition

$$k_B T_c = \frac{\pi}{2} \rho_s. \quad (30)$$

As finite temperature can roughly be interpreted as a source of disorder, our conclusions should be robust against disorder, inherent to experiments.

#### V. DENSITY OF STATES AND BETHE-SALPETER EQUATION

The density of states (DOS) is given by the following expression:

$$\nu(\mu) = \frac{g_s}{N_c} \sum_{\mathbf{k}, n} \delta(\epsilon_{\mathbf{k}, n} - \mu), \quad (31)$$



with  $g_s = 2$  denoting the spin-degeneracy and  $N_c$  the number of unit cells. Whereas the self-consistency procedure is done with  $N_c = 36$ , the DOS is calculated with  $N_c = 900$  that already yield well-converged curves. The results for different twist angles are shown in Fig. 8, where the vertical dashed lines indicate that chemical potential at optimal doping  $n/n_0 = -2.4$ .

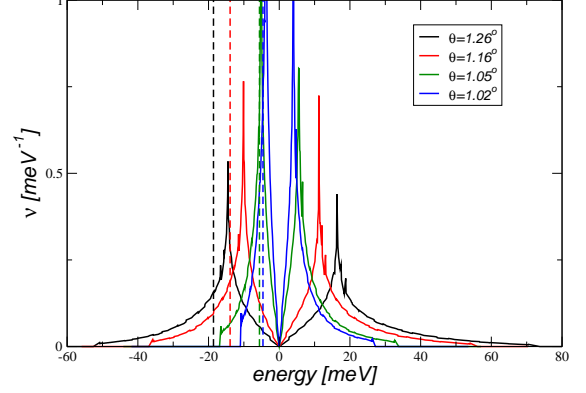


FIG. 8. DOS for various twist angles at  $T = 0$  (solid lines). The vertical dashed lines indicate the chemical potential at optimal doping  $n/n_0 = -2.4$ .

We will now show how the DOS defines the pairing amplitude of the Cooper-pairs. For that, we first consider a general bare interaction vertex  $\Gamma^0(p_1 p_2; p_3 p_4)$  with  $p_i = (i p_0, \mathbf{p})$ . The total two-particle interaction vertex includes the infinite sum of repeated ladder interactions and can be written in its self-consistent form as follows:

$$\Gamma(p_1 p_2; p_3 p_4) = \Gamma^0(p_1 p_2; p_3 p_4) + \frac{k_B T}{N_c} \sum_q \Gamma^0(p_1 p_2; p_3 + q, p_4 - q) G^0(p_1 - q) G^0(p_2 + q) \Gamma(p_1 - q, p_2 + q; p_3 p_4), \quad (32)$$

where the non-interacting Green's function reads  $G^0(p) = 1/(i\hbar p_0 - \epsilon_{\mathbf{p}})$ .

The above Bethe-Salpeter equation of the particle-particle channel is shown diagrammatically in Fig. 9. For a *static* initial interaction  $\Gamma^0(p_1 p_2; p_3 p_4) = \Gamma^0(\mathbf{p}_1 \mathbf{p}_2; \mathbf{p}_3 \mathbf{p}_4)$ , the integral over the frequency decouples. If  $\Gamma^0$  is further momentum independent, i.e., a contact potential with  $\Gamma^0(\mathbf{p}_1 \mathbf{p}_2; \mathbf{p}_3 \mathbf{p}_4) \rightarrow g$ , the full vertex only depends on the energy/momentum transfer  $p$ , i.e.,  $\Gamma(p_1 p_2; p_3 p_4) \rightarrow \Gamma(0 p; p 0) \equiv \Gamma(p)$ . In this case, the Bethe-Salpeter equation is considerably simplified and reads

$$\Gamma(p) = g + g \frac{k_B T}{N_c} \sum_q G^0(-q) G^0(p + q) \Gamma(p + q). \quad (33)$$

For the static Cooper channel, we will set  $p = 0$  and the full vertex becomes momentum independent, leading to the solution

$$\Gamma = \frac{g}{1 + g \frac{k_B T}{N_c} \sum_q G^0(-q) G^0(q)}. \quad (34)$$

The vertex is thus determined by the summation of the

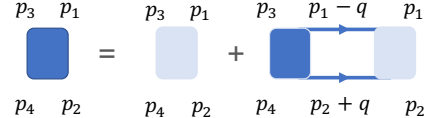


FIG. 9. Self-consistent Bethe-Salpeter equation of the particle-particle channel for a general bare vertex (light blue square).

Cooper channel and the summation of the Matsubara frequencies yields the following result:

$$\frac{k_B T}{N_c} \sum_q G^0(-q) G^0(q) = \frac{1}{N_c} \sum_q \frac{1 - 2f(\epsilon_q)}{2\epsilon_q}, \quad (35)$$

where we introduced the Fermi function  $f$  with  $\mu = 0$  and assumed particle-hole symmetry  $\epsilon_q = \epsilon_{-q}$ . With the

DOS  $\nu$ , we can write

$$\frac{k_B T}{N_c} \sum_q G^0(-q) G^0(q) = \int_{\Lambda_B}^{\Lambda_B} d\epsilon \nu(\epsilon) \frac{1 - 2f(\epsilon)}{2\epsilon} \quad (36)$$

$$\rightarrow \nu \int_{k_B T}^{\Lambda_B} \frac{d\epsilon}{\epsilon} = \nu \ln(\Lambda_B / k_B T) ,$$

where we introduced a band cutoff  $\Lambda_B$  and also assumed that the DOS is approximately constant in this regime. Obviously, a constant DOS is not a good approximation in the case of TBG, but we will keep it for sake of sim-

plicity.

The critical temperature is now defined when the perturbative approach breaks down. This gives the following expression:

$$k_B T_c = \Lambda_B \exp\left(-\frac{1}{g\nu}\right) \quad (37)$$

This functional behavior thus only depends on the DOS at optimal doping  $n/n_0 = -2.4$  and the contact potential which we can choose to be less or of the order of the bandwidth, i.e.,  $g = 5\text{meV}$ .

- 
- <sup>1</sup> Y. Cao, V. Fatemi, S. Fang, K. Watanabe, T. Taniguchi, E. Kaxiras, and P. Jarillo-Herrero, *Nature* **556**, 43 (2018).
  - <sup>2</sup> M. Yankowitz, S. Chen, H. Polshyn, Y. Zhang, K. Watanabe, T. Taniguchi, D. Graf, A. F. Young, and C. R. Dean, *Science* **363**, 1059 (2019).
  - <sup>3</sup> P. Stepanov, I. Das, X. Lu, A. Fahimniya, K. Watanabe, T. Taniguchi, F. H. L. Koppens, J. Lischner, L. Levitov, and D. K. Efetov, *Nature* **583**, 375 (2020).
  - <sup>4</sup> E. Khalaf, A. J. Kruchkov, G. Tarnopolsky, and A. Vishwanath, *Phys. Rev. B* **100**, 085109 (2019).
  - <sup>5</sup> C. Mora, N. Regnault, and B. A. Bernevig, *Phys. Rev. Lett.* **123**, 026402 (2019).
  - <sup>6</sup> J. M. Park, Y. Cao, K. Watanabe, T. Taniguchi, and P. Jarillo-Herrero, *Nature* **590**, 249 (2021).
  - <sup>7</sup> Z. Hao, A. M. Zimmerman, P. Ledwith, E. Khalaf, D. H. Najafabadi, K. Watanabe, T. Taniguchi, A. Vishwanath, and P. Kim, *Science* **371**, 1133 (2021).
  - <sup>8</sup> Y. Cao, J. M. Park, K. Watanabe, T. Taniguchi, and P. Jarillo-Herrero, *Nature* **595**, 526 (2021).
  - <sup>9</sup> M. Christos, S. Sachdev, and M. S. Scheurer, *Phys. Rev. X* **12**, 021018 (2022).
  - <sup>10</sup> J. M. Park, Y. Cao, L.-Q. Xia, S. Sun, K. Watanabe, T. Taniguchi, and P. Jarillo-Herrero, *Nature Materials* **21**, 877 (2022).
  - <sup>11</sup> H. Kim, Y. Choi, É. Lantagne-Hurtubise, C. Lewandowski, A. Thomson, L. Kong, H. Zhou, E. Baum, Y. Zhang, L. Holleis, K. Watanabe, T. Taniguchi, A. F. Young, J. Alicea, and S. Nadj-Perge, *Nature* **623**, 942 (2023).
  - <sup>12</sup> J. González and T. Stauber, *Nature Communications* **14**, 2746 (2023).
  - <sup>13</sup> A. Uri, S. C. de la Barrera, M. T. Randeria, D. Rodan-Legrain, T. Devakul, P. J. D. Crowley, N. Paul, K. Watanabe, T. Taniguchi, R. Lifshitz, L. Fu, R. C. Ashoori, and P. Jarillo-Herrero, *Nature* **620**, 762 (2023).
  - <sup>14</sup> N. Nakatsuji, T. Kawakami, and M. Koshino, *Phys. Rev. X* **13**, 041007 (2023).
  - <sup>15</sup> C. Yang, J. May-Mann, Z. Zhu, and T. Devakul, *Phys. Rev. B* **110**, 115434 (2024).
  - <sup>16</sup> X. Zhang, K.-T. Tsai, Z. Zhu, W. Ren, Y. Luo, S. Carr, M. Lusk, E. Kaxiras, and K. Wang, *Phys. Rev. Lett.* **127**, 166802 (2021).
  - <sup>17</sup> B. Lian, Z. Wang, and B. A. Bernevig, *Phys. Rev. Lett.* **122**, 257002 (2019).
  - <sup>18</sup> P. Törmä, S. Peotta, and B. A. Bernevig, *Nature Reviews Physics* **4**, 528 (2022).
  - <sup>19</sup> M. Sánchez Sánchez and T. Stauber, *Phys. Rev. B* **109**, 195167 (2024).
  - <sup>20</sup> B. Putzer and M. S. Scheurer, *Phys. Rev. B* **111**, 144513 (2025).
  - <sup>21</sup> Y. Cao, D. Rodan-Legrain, J. M. Park, N. F. Q. Yuan, K. Watanabe, T. Taniguchi, R. M. Fernandes, L. Fu, and P. Jarillo-Herrero, *Science* **372**, 264 (2021).
  - <sup>22</sup> Y. Choi, H. Kim, C. Lewandowski, Y. Peng, A. Thomson, R. Polski, Y. Zhang, K. Watanabe, T. Taniguchi, J. Alicea, and S. Nadj-Perge, *Nature Physics* **17**, 1375 (2021).
  - <sup>23</sup> X. Wang and O. Vafek, *Phys. Rev. X* **14**, 021042 (2024).
  - <sup>24</sup> M. Bocarsly, I. Roy, V. Bhardwaj, M. Uzan, P. Ledwith, G. Shavit, N. Banu, Y. Zhou, Y. Myasoedov, K. Watanabe, T. Taniguchi, Y. Oreg, D. E. Parker, Y. Ronen, and E. Zeldov, *Nature Physics* **21**, 421 (2025).
  - <sup>25</sup> See Supplemental Information for details on the self-consistent algorithm conserving the valley charge, a symmetry analysis for the coupling parameters, the calculation of the Drude weight and density of states as well as additional plots of the band structure.
  - <sup>26</sup> J. González and T. Stauber, *Phys. Rev. Lett.* **122**, 026801 (2019).
  - <sup>27</sup> J. González, F. Guinea, and M. Vozmediano, *Nuclear Physics B* **424**, 595 (1994).
  - <sup>28</sup> D. C. Elias, R. V. Gorbachev, A. S. Mayorov, S. V. Morozov, A. A. Zhukov, P. Blake, L. A. Ponomarenko, I. V. Grigorieva, K. S. Novoselov, F. Guinea, and A. K. Geim, *Nat Phys* **7**, 701 (2011).
  - <sup>29</sup> G. Li, A. Luican, and E. Y. Andrei, *Phys. Rev. Lett.* **102**, 176804 (2009).
  - <sup>30</sup> J. Chae, S. Jung, A. F. Young, C. R. Dean, L. Wang, Y. Gao, K. Watanabe, T. Taniguchi, J. Hone, K. L. Shepard, P. Kim, N. B. Zhitenev, and J. A. Stroscio, *Phys. Rev. Lett.* **109**, 116802 (2012).
  - <sup>31</sup> D. A. Siegel, C.-H. Park, C. Hwang, J. Deslippe, A. V. Fedorov, S. G. Louie, and A. Lanzara, *Proceedings of the National Academy of Sciences* **108**, 11365 (2011).
  - <sup>32</sup> G. L. Yu, R. Jalil, B. Belle, A. S. Mayorov, P. Blake, F. Schedin, S. V. Morozov, L. A. Ponomarenko, F. Chiappini, S. Wiedmann, U. Zeitler, M. I. Katsnelson, A. K. Geim, K. S. Novoselov, and D. C. Elias, *Proceedings of the National Academy of Sciences* **110**, 3282 (2013).
  - <sup>33</sup> C. Faugeras, S. Berciaud, P. Leszczynski, Y. Henni, K. Nogajewski, M. Orlita, T. Taniguchi, K. Watanabe, C. Forsythe, P. Kim, R. Jalil, A. K. Geim, D. M. Basko, and M. Potemski, *Phys. Rev. Lett.* **114**, 126804 (2015).
  - <sup>34</sup> P. R. Whelan, Q. Shen, B. Zhou, I. G. Serrano, M. V. Kamalakar, D. M. A. Mackenzie, J. Ji, D. Huang, H. Shi,

- D. Luo, M. Wang, R. S. Ruoff, A.-P. Jauho, P. U. Jepsen, P. Bøggild, and J. M. Caridad, *2D Materials* **7**, 035009 (2020).
- <sup>35</sup> M. Lee, I. Das, J. Herzog-Arbeitman, J. Papp, J. Li, M. Daschner, Z. Zhou, M. Bhatt, M. Currle, J. Yu, Y. Jiang, M. Becherer, R. Mittermeier, P. Altpeter, C. Obermayer, H. Lorenz, G. Chavez, B. T. Le, J. Williams, K. Watanabe, T. Taniguchi, B. A. Bernevig, and D. K. Efetov, “Revealing electron-electron interactions in graphene at room temperature with the quantum twisting microscope,” (2025), arXiv:2507.03189 [cond-mat.mes-hall].
- <sup>36</sup> J. González, F. Guinea, and M. A. H. Vozmediano, *Phys. Rev. B* **59**, R2474 (1999).
- <sup>37</sup> T. Stauber, F. Guinea, and M. A. H. Vozmediano, *Phys. Rev. B* **71**, 041406 (2005).
- <sup>38</sup> E. G. Mishchenko, *Phys. Rev. Lett.* **98**, 216801 (2007).
- <sup>39</sup> D. E. Sheehy and J. Schmalian, *Phys. Rev. Lett.* **99**, 226803 (2007).
- <sup>40</sup> I. F. Herbut, V. Juricic, and O. Vafek, *Phys. Rev. Lett.* **100**, 046403 (2008).
- <sup>41</sup> O. Vafek and M. J. Case, *Phys. Rev. B* **77**, 033410 (2008).
- <sup>42</sup> J. Jung and A. H. MacDonald, *Phys. Rev. B* **84**, 085446 (2011).
- <sup>43</sup> M. Trushin and J. Schliemann, *Phys. Rev. Lett.* **107**, 156801 (2011).
- <sup>44</sup> A. Giuliani, V. Mastropietro, and M. Porta, *Annals of Physics* **327**, 461 (2012).
- <sup>45</sup> E. Barnes, E. H. Hwang, R. E. Throckmorton, and S. Das Sarma, *Phys. Rev. B* **89**, 235431 (2014).
- <sup>46</sup> N. Y. Astrakhsantsev, V. V. Braguta, and M. I. Katsnelson, *Phys. Rev. B* **92**, 245105 (2015).
- <sup>47</sup> C. Bauer, A. Rückriegel, A. Sharma, and P. Kopietz, *Phys. Rev. B* **92**, 121409 (2015).
- <sup>48</sup> A. Sharma and P. Kopietz, *Phys. Rev. B* **93**, 235425 (2016).
- <sup>49</sup> T. Stauber, P. Parida, M. Trushin, M. V. Ulybyshev, D. L. Boyda, and J. Schliemann, *Phys. Rev. Lett.* **118**, 266801 (2017).
- <sup>50</sup> J. Kang and O. Vafek, *Phys. Rev. Lett.* **122**, 246401 (2019).
- <sup>51</sup> K. Seo, V. N. Kotov, and B. Uchoa, *Phys. Rev. Lett.* **122**, 246402 (2019).
- <sup>52</sup> N. Bultinck, E. Khalaf, S. Liu, S. Chatterjee, A. Vishwanath, and M. P. Zaletel, *Phys. Rev. X* **10**, 031034 (2020).
- <sup>53</sup> Z.-D. Song, B. Lian, N. Regnault, and B. A. Bernevig, *Phys. Rev. B* **103**, 205412 (2021).
- <sup>54</sup> B. A. Bernevig, Z.-D. Song, N. Regnault, and B. Lian, *Phys. Rev. B* **103**, 205413 (2021).
- <sup>55</sup> B. Lian, Z.-D. Song, N. Regnault, D. K. Efetov, A. Yazdani, and B. A. Bernevig, *Phys. Rev. B* **103**, 205414 (2021).
- <sup>56</sup> D. Călugăru, N. Regnault, M. Oh, K. P. Nuckolls, D. Wong, R. L. Lee, A. Yazdani, O. Vafek, and B. A. Bernevig, *Phys. Rev. Lett.* **129**, 117602 (2022).
- <sup>57</sup> G. Wagner, Y. H. Kwan, N. Bultinck, S. H. Simon, and S. A. Parameswaran, *Phys. Rev. Lett.* **128**, 156401 (2022).
- <sup>58</sup> J. M. B. L. dos Santos, N. M. R. Peres, and A. H. C. Neto, *Physical Review Letters* **99** (2007).
- <sup>59</sup> G. Li, A. Luican, J. M. B. Lopes dos Santos, A. H. Castro Neto, A. Reina, J. Kong, and E. Y. Andrei, *Nature Physics* **6**, 109 (2010).
- <sup>60</sup> E. Suárez Morell, J. D. Correa, P. Vargas, M. Pacheco, and Z. Barticevic, *Phys. Rev. B* **82**, 121407 (2010).
- <sup>61</sup> R. Bistritzer and A. H. MacDonald, *Proceedings of the National Academy of Sciences* **108**, 12233 (2011).
- <sup>62</sup> M. Sánchez Sánchez, J. González, and T. Stauber, *Phys. Rev. B* **111**, 205133 (2025).
- <sup>63</sup> M. Koshino, N. F. Q. Yuan, T. Koretsune, M. Ochi, K. Kuroki, and L. Fu, *Phys. Rev. X* **8**, 031087 (2018).
- <sup>64</sup> P. Moon and M. Koshino, *Phys. Rev. B* **87**, 205404 (2013).
- <sup>65</sup> R. E. Throckmorton and O. Vafek, *Phys. Rev. B* **86**, 115447 (2012).
- <sup>66</sup> Y. Saito, J. Ge, K. Watanabe, T. Taniguchi, and A. F. Young, *Nature Physics* **16**, 926 (2020).
- <sup>67</sup> A. Ceferino and F. Guinea, *2D Materials* **11**, 035015 (2024).
- <sup>68</sup> H. Suzuura and T. Ando, *Phys. Rev. B* **65**, 235412 (2002).
- <sup>69</sup> M. M. A. Ezzi, G. N. Pallewela, C. De Beule, E. J. Mele, and S. Adam, *Phys. Rev. Lett.* **133**, 266201 (2024).
- <sup>70</sup> S. Carr, S. Fang, Z. Zhu, and E. Kaxiras, *Phys. Rev. Res.* **1**, 013001 (2019).
- <sup>71</sup> J. Kang and O. Vafek, *Phys. Rev. B* **107**, 075408 (2023).
- <sup>72</sup> F. Guinea and N. R. Walet, *Phys. Rev. B* **99**, 205134 (2019).
- <sup>73</sup> O. Vafek and J. Kang, *Phys. Rev. Lett.* **125**, 257602 (2020).
- <sup>74</sup> W. Miao, C. Li, X. Han, D. Pan, and X. Dai, *Phys. Rev. B* **107**, 125112 (2023).